Colloidal asphaltene deposition in laminar pipe flow: Flow rate and parametric effects

S. M. Hashmi,[a)] M. Loewenberg, and A. Firoozabadi[b)]
Department of Chemical and Environmental Engineering, Yale University, New Haven, Connecticut 06510, USA

Deposition from a suspended phase onto a surface can aversely affect everyday transport processes on a variety of scales, from mineral scale corrosion of household plumbing systems to asphaltene deposition in large-scale pipelines in the petroleum industry. While petroleum may be a single fluid phase under reservoir conditions, depressurization upon production often induces a phase transition in the fluid, resulting in the precipitation of asphaltene material which readily aggregates to the colloidal scale and deposits on metallic surfaces. Colloidal asphaltene deposition in wellbores and pipelines can be especially problematic for industrial purposes, where cleanup processes necessitate costly operational shutdowns. In order to better understand the parametric dependence of deposition which leads to flow blockages, we carry out lab-scale experiments under a variety of material and flow conditions. We develop a parametric scaling model to understand the fluid dynamics and transport considerations governing deposition. The lab-scale experiments are performed by injecting precipitating petroleum fluid mixtures into a small metal pipe, which results in deposition and clogging, assessed by measuring the pressure drop across the pipe. Parametric scaling arguments suggest that the clogging behavior is determined by a combination of the Peclet number, volume fraction of depositing material, and the volume of the injection itself. © *2015 AIP Publishing LLC.*
[http://dx.doi.org/10.1063/1.4927221]

I. INTRODUCTION

Asphaltenes, the most aromatic component of petroleum fluid, defined as being insoluble in medium chain alkanes and soluble in aromatics, have a tendency to precipitate out of petroleum fluids under a variety of conditions. The precipitation or phase separation process involves molecular asphaltene association and growth of nanoparticles, followed by rapid colloidal aggregation to macro-scopic scales, and complete separation by sedimentation or deposition.[1,2] Colloidal asphaltene deposition on metal surfaces causes problems in industrial settings: as petroleum fluids are produced from reservoirs, depressurization causes asphaltene precipitation, ultimately resulting in deposition in wellbores and pipelines. Such deposition can impede production. Lengthy and costly shutdowns are often required to restore full operation. Asphaltene deposits can be removed by the addition of large amounts of aromatic solvents, but this process is costly due to the amount of chemicals required. The purpose of this paper is to describe the fluid dynamics and transport principles which govern colloidal asphaltene deposition under laminar flow conditions.

Understanding colloidal deposition in convective flows impacts a variety of industries. Convection can be exploited to assemble thin evaporating films of particulate suspensions into structured coatings for a variety of applications.[3,4] Understanding the physics governing particle deposition in laminar flow conditions can be exploited to improve biosensor measurements.[5] Convective deposition in complex branched geometries plays an important role in both disease and drug-delivery processes in

---

a)Electronic mail: sara.hashmi@yale.edu.
b)Electronic mail: abbas.firoozabadi@yale.edu.

27, 083302-1

the nasal passages and airways.[6,7] Similarly, a better understanding of colloidal asphaltene deposition in metal pipes can inform potential preventive measures for the petroleum industry.

During petroleum production, asphaltene deposits can build up both in vertical tubing and in horizontal pipes. A few case studies have been performed to measure the thickness of the deposited layer in pipes with diameters between 2 and 5 inches, and researches found that the deposit thickness reached between 1/3 and 2/3 of the pipe radius.[8,9] Such excessive deposition greatly reduces production efficiency. As a result, better understanding of the deposition process has been sought through modeling efforts. Most models of asphaltene deposition include thermodynamic descriptions of asphaltene solubility in addition to transport and thus require a variety of adjustable parameters. In one, asphaltenes are assumed to precipitate and deposit based on the known thermodynamics conditions in two different wells in Southeast Mexico.[10] In another, an Arrhenius model was used to describe the deposition rate of asphaltene on the surface of a pipe.[11] A third attempt incorporated the thermodynamic behavior of asphaltene precipitation into a deposition simulator, using the PC-SAFT (Perturbed-Chain Statistical Associating Fluid Theory) equation of state to predict precipitation coupled with a diffusively driven deposition model.[12] Despite these thermodynamic modeling efforts, a simple and quantitative understanding of the transport factors affecting colloidal asphaltene deposition in laminar flows remains lacking.

On the lab scale, several experimental works have investigated asphaltene deposition in a variety of geometries. Experimental asphaltene deposition inside a Couette cell has been modeled by accounting for centrifugal forces in turbulent flows.[13] Experiments in microfluidic glass capillaries investigated asphaltene deposition in very low-Reynolds number flows.[14,15] In this case, colloidal-sized asphaltene aggregates were observed to exhibit stick-and-roll behavior, and molecular dynamics simulations captured several important features of the experimental observations.[15] In straight metal capillary studies, pressure drop is monitored as an indication of the constriction of the conduit.[16,17] One study using a fixed flow rate and changing ratios of heptane to two different petroleum fluids concluded that the amount of precipitating material is a strong contributor to the deposition behavior: when too little heptane was added to the petroleum fluid, very little deposition occurred; while the largest amount of heptane used, 50% by volume, generated the most deposition.[16] In larger metal pipes (24 mm diameter), decreasing flow rate and increasing asphaltene content were both found to increase deposition, but the control parameters were varied only by a factor of two.[11] Attempts to rescale raw pressure-drop data using material parameters fail to fully collapse the data.[16] Furthermore, there is disagreement regarding the uniformity of deposition along the axial direction in a pipe. Evidence has been presented to suggest both that deposition is uniform throughout a given length of pipe and also that deposition occurs mainly near the pipe inlet.[16,18] Despite the available experimental data, theoretical formulations explaining the fluid dynamics and transport phenomena governing asphaltene deposition remain lacking.

We investigate asphaltene deposition in lab-scale capillary pipelines and provide a simple scaling model to account for our observations. We induce asphaltene precipitation by adding heptane to a petroleum fluid and inject the mixture through a small metal pipe. We assess the deposition of asphaltenes as a function of various parameters including flow rate, pipe geometry, and petroleum fluid composition. We provide a parametric scaling argument based on diffusion-driven deposition, which predicts increasing deposition, and thus increasing pressure drop, as either asphaltene content is increased or flow rate is decreased. The diffusively driven deposition model is simple, yet robust: it describes data collected over a wide range of governing parameters, including more than one order of magnitude in both flow rate and asphaltene content. We observe and describe the effect of ablation by shear in limiting the growth of the deposit at low flow rates. In this model, we neglect the axial dependence of asphaltene deposition, and the agreement with experimental results supports the validity of this assumption. We address the thermodynamic considerations of asphaltene precipitation by directly measuring the precipitated asphaltene content. Once this quantity is known, the agreement of the model with the data demonstrates how transport considerations, rather than thermodynamics, govern the resulting asphaltene deposition dynamics.

TABLE I. Material properties: viscosity of the petroleum fluids and their asphaltene content. The asphaltene mass fraction f is extracted from the petroleum fluids by a standard procedure which involves filtering mixtures of 1 g of petroleum fluid in 40 ml of heptane. The Newtonian viscosity μ for each fluid is assessed in a rheometer.

Petroleum fluid	μ (cP)	f
M2	20.9	0.0446 ± 0.0023
M2Tol	1.9	0.0248 ± 0.0024
CVA	32.7	0.0770 ± 0.0051
BAB	5.1	0.0032 ± 0.0004

II. MATERIALS AND METHODS

A. Materials

We use four different petroleum fluids, as tabulated in Table I, to assess asphaltene deposition in the metal pipes. The petroleum fluids are labeled M2, M2Tol, CVA, and BAB and have their sources at various fields around the world, from Mexico to the Persian Gulf. The petroleum fluid M2Tol is a mixture of M2 and toluene in equal parts by volume. We characterize the petroleum fluids by their asphaltene fraction f and viscosity μ. We measure ρ (g/ml) using a densitometer (Anton Paar DMA 5000). We measure f via filtration, both by the standard filtration method, and at the composition conditions encountered in the pipe. For the standard measurement, 1 g of petroleum fluid is mixed with 40 ml of heptane (HPLC grade, JT Baker), allowed to precipitate overnight between 18 and 24 h, and then filtered to recover the asphaltene fraction f. To measure f at the conditions encountered in the pipe flow experiments, we mix each petroleum fluid with heptane using the volume ratios given in Table II and denote this quantity as f_p. The values in Table I, for f, and in Table II, for f_p, indicate averages of as many as 40 different filtration measurements. Overall for each of the four fluids, f_p, as measured using the pipe conditions, is roughly 30% less than f, measured at the higher dilution of 40 ml heptane per gram petroleum fluid. At times, we will use f_p as a descriptor of the petroleum fluid mixtures assessed.

To assess deposition, we inject four different precipitating mixtures through three different pipes. Table II indicates the mixtures used: Mixture A is composed of equal volumes of heptane and petroleum fluid M2; Mixture B is composed of 25% M2, 25% toluene, and 50% heptane by volume; Mixture C is an equal volume mixture of CVA with heptane; and Mixture D is heptane mixed with BAB in a volume ratio of 2:1. Initial experimentation using a range of heptane volume ratios and flow rates was used to determine the appropriate mixture ratios to ensure deposition. In the case of petroleum fluid BAB, these initial tests were extensive.

We measure the viscosity μ using a rheometer (Anton Paar MCR 301), in a cone-and-plate geometry (CP25), over a range of shear rates $\dot{\gamma}$. Fig. 1 shows the rheological behavior of the three petroleum fluids and mixtures of those fluids with heptane. The four petroleum fluids are Newtonian,

TABLE II. Deposition mixtures. The mixtures, labeled A, B, C, and D, are described, giving the petroleum fluid and heptane ratio employed in each mixture, as well as f_P, the measured asphaltene fraction for each of the compositions. Mixtures A and C are equivolume mixtures of heptane with M2 and CVA, respectively. The total volume composition of Mixture B is 25% M2, 25% toluene, and 50% heptane. Mixture D has a 2:1 volume ratio of heptane to BAB.

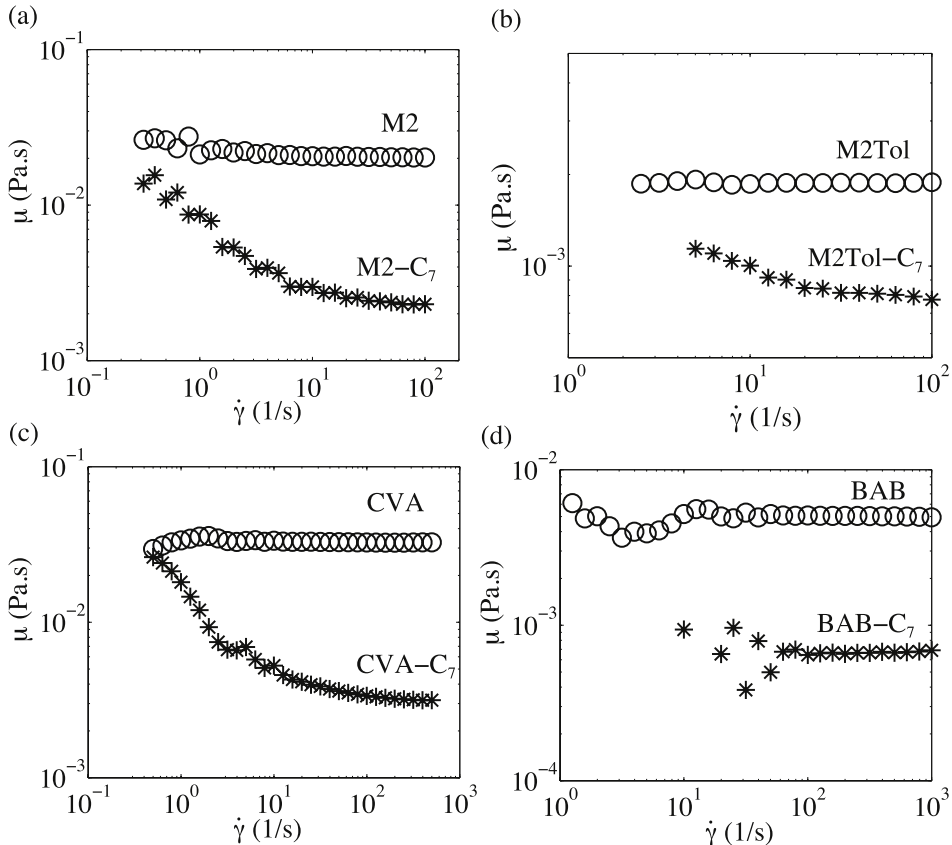| Mixture	Petroleum fluid	Heptane:PF ratio	f_P
A	M2	1:1	0.0301 ± 0.0050
B	M2Tol	1:1	0.0190 ± 0.0031
C	CVA	1:1	0.0504 ± 0.0055
D	BAB	2:1	0.0021 ± 0.0006

FIG. 1. Bulk rheological characteristics. (a)–(d) each show μ as a function of $\dot{\gamma}$ for both the petroleum fluids and their mixtures with heptane. In each, the open circles indicate the petroleum fluid and the stars indicate a mixture with heptane. (a) shows results for M2 and Mixture A, (b) shows results for M2Tol and Mixture B, (c) shows results for CVA and Mixture C, and (d) shows results for BAB and Mixture D.

as shown by the open circles in each plot: M2 in (a), M2Tol in (b), CVA in (c), and BAB in (d). Mixture A, the equi-volume mixture of M2 with heptane, shear thins in the range $0.3 < \dot{\gamma} < {\sim}50 \text{ s}^{-1}$, as seen in Fig. 1(a). Between 50 and 100 s^{-1}, μ for Mixture A is approximately an order of magnitude less than for M2 on its own. Mixture B, which is composed of 25% M2, 25% toluene, and 50% heptane by volume, exhibits slightly shear-thinning behavior, as seen in Fig. 1(b). The equi-volume mixture of CVA and heptane, Mixture C, like Mixture A, shear thins below ${\sim}100 \text{ s}^{-1}$, as seen in Fig. 1(c). At $\dot{\gamma} = 500 \text{ s}^{-1}$, μ for Mixture C is also approximately an order of magnitude less than CVA itself. Asphaltene precipitation is known to result in unstable, quickly aggregating suspensions.[2] The shear-thinning in Mixtures A and C is due to the shear-induced breakup of the unstable colloidal suspension, as has been observed in colloidal gels.[19,20] Mixture D, the mixture of 1 part BAB with 2 parts heptane, however, does not strongly exhibit any shear-thinning behavior, as seen in Fig. 1(d). In this case, due to the low asphaltene content of BAB, and the higher dilution with heptane, the resulting colloidal suspension is simply too dilute to exhibit rheological signatures.

B. Methods

In this study, we employ three different stainless steel pipes (McMaster-Carr) of different geometries, as indicated in Table III, which lists the lengths L (cm), internal radii R_0 (cm), cross sectional areas A (cm^2), and volumes V (ml). Pipes 1 and 2 are the same length with different radii, while Pipes 2 and 3 have the same radius but different lengths. Flow is driven through the pipes at a constant volume flow rate Q, using syringe pumps (Legato 200, KD Scientific), and a pressure transducer (PX409, Omega Engineering) is placed at the inlet of the pipe to measure the total pressure drop ΔP.

TABLE III. Pipe geometries.

Pipe	R_0 (cm)	L (cm)	A (cm^2)	V (ml)
1	0.05	30	0.0079	0.24
2	0.03	30	0.0028	0.08
3	0.03	71	0.0028	0.20

The outlet of the pipe is open to atmospheric pressure. A schematic of the setup is given in Fig. 2(a). Fig. 2(b) shows an exploded image of the junction, including a small metal nozzle that is inserted in the heptane line to enhance mixing in the T-junction. The brass compression fitting seen in the bottom of Fig. 2(b) indicates the position of the transducer, located on the heptane flow line before the T-junction. Visual inspection confirms deposition throughout the length of the pipe. Fig. 2(c) shows three images of Pipe 1, which was cut after the final injection of a depositing asphaltene mixture, Mixture C. The top and center images show cutaways of the cross section, at a distance of <1 cm from the inlet and roughly 2/3 the pipe length, respectively. The bottom image shows asphaltenes deposited at the outlet. Between experimental runs, we dismantle the pipe, transducer, and nozzle and rinse all parts with toluene to dissolve any deposited asphaltenes. The rinse is performed until the toluene runs clear and colorless through all components. The run-to-run reproducibility of the deposition measurements confirms removal of the asphaltene deposits.

Table IV indicates the pipes used for each mixture, as well as the range of flow conditions as described by the flow rate Q (ml/h), shear rate $\dot{\gamma}$ (s^{-1}), the pipe Reynolds number $Re = 2\rho Q R_0/A\mu$, and the Peclet number

$$Pe = \frac{Q}{R_0 D}. \tag{1}$$

We estimate the diffusion coefficient D using the Stokes-Einstein relation $D = k_B T/6\pi\mu a$, where μ is the viscosity of the suspending fluid, $a = 100$ nm is size of the depositing particles, $T = 25\,°C$ the temperature, and k_B the Boltzmann constant. While asphaltenes have a tendency to aggregate to
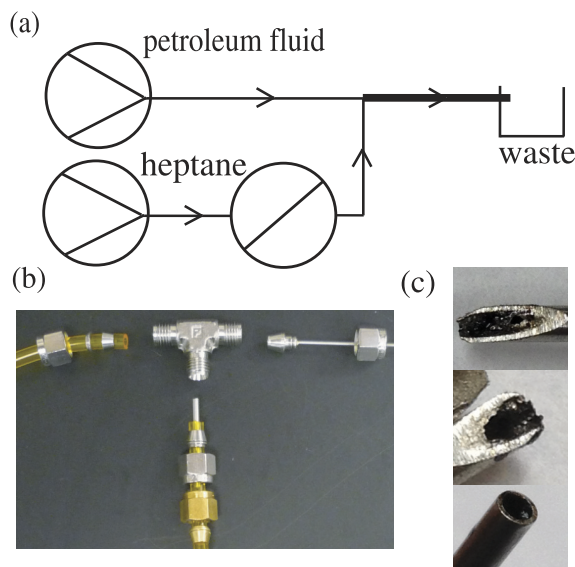

FIG. 2. Flow setup and schematic: (a) shows a diagram of the setup, from the syringe pump inputs (each labeled with the fluid it carries) to the output waste. The pressure transducer is located on the heptane fluid line before the T-junction. (b) shows a picture of the nozzle employed at the T-junction in (a) which allows for better mixing of the two fluids. The brass compression fitting seen in the bottom of (b) indicates the relative position of the transducer directly before the T-junction. (c) shows example images of asphaltene buildup in Pipe 1 after an injection of a depositing mixture. The top image shows Pipe 1 cut within 1 cm beyond the inlet, the middle image shows a cut at approximately 2/3 of its length, and the bottom image shows the outlet of the pipe, all after the same injection.

TABLE IV. Flow conditions for each mixture injected in the given pipes. The columns indicating Q (ml/h), $\dot{\gamma}$ (s^{-1}), Re, and Pe give the ranges of experimental conditions investigated.

Mixture	Pipe(s)	Q (ml/h)	$\dot{\gamma}$ (s^{-1})	Pe	Re
A	1	6-400	13-890	$2 \times 10^6 - 1 \times 10^8$	0.9–62
B	1	6-400	13-890	$8 \times 10^5 - 5 \times 10^7$	1.3–82
C	1, 2, 3	4-400	10-890	$2 \times 10^6 - 7 \times 10^7$	0.4–43
D	1, 2	6.6	15-70	$6 \times 10^5 - 1 \times 10^6$	3–5

the colloidal scale, several hundred nm and beyond, dynamic light scattering measurements suggest that aggregation to a few hundred nm happens very quickly, within seconds after mixing petroleum fluids with heptane.[2] We choose $a = 100$ nm to reflect that asphaltenes may deposit even before fully aggregating to a larger scale.

In order to validate the pipe flow setup, we run several control experiments. In the first control experiment, we flow a pure petroleum fluid through the pipe to ensure that asphaltene deposition does not occur. Fig. 3(a) shows the resulting constant pressure drop ΔP for the CVA and BAB fluids, both flowing in Pipe 2. For CVA, $Q = 42$ ml/h, while for BAB, $Q = 6.6$ ml/h. Given the same injection volume for each fluid, but different flow rates, we plot ΔP as a function of the dimensionless time
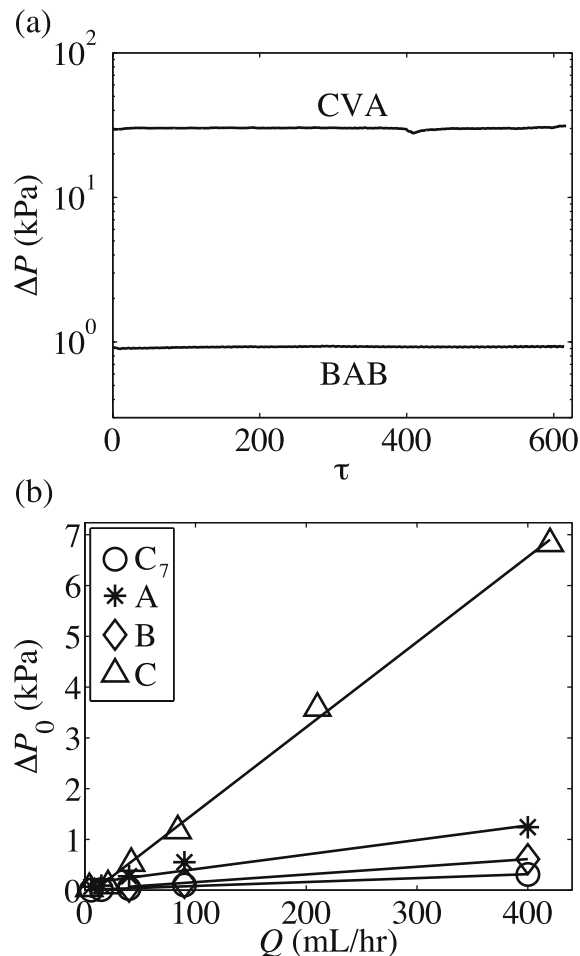

FIG. 3. Control runs. The traces in (a) demonstrate that the petroleum fluids on their own do not generate deposition, as demonstrated by CVA at $Q = 42$ ml/h in Pipe 3 and BAB at $Q = 6.6$ ml/h in Pipe 2. (b) indicates ΔP_0 as a function of Q in ml/h, for heptane, labeled C_7, and before the onset of deposition for the three mixtures as indicated in the legend. All data in (b) are as measured in Pipe 1.

$\tau = Qt/V$. V is the pipe volume, such that τ means the number of times the pipe has been completely filled, denoting the number of pore volumes injected through the pipe. In the second control, we validate that the flow is laminar, governed by the Poiseuille equation,

$$\frac{\Delta P}{L} = \frac{8\mu Q}{\pi R^4}, \tag{2}$$

where μ is the viscosity of the fluid mixture. We flow heptane alone through the pipe at different flow rates and measure the pressure drop as a function of Q. The result is linear, as expected, with a slope 8.3×10^{-4} (kPa/(ml/h)). The expected value of the slope of $\Delta P(Q)$ for heptane, given by Eq. (2), is approximately 40% higher: 1.3×10^{-3} (kPa/(ml/h)). To further validate the use of Eq. (2), we also investigate a series of runs of depositing mixtures at different flow rates and measure ΔP_0, the initial pressure drop before the onset of deposition. In each case, for Mixtures A, B, and C, ΔP_0 is linear with Q, as expected for a clean pipe prior to deposition. Fig. 3(b) shows the results for $\Delta P_0(Q)$ for heptane and three of the depositing mixtures, as indicated in the legend. The solid lines are measured slopes of the data. Comparing the measured slopes to those predicted by Eq. (2), the deviations range from 30% to 70%. These discrepancies could arise from the T-junction, which is located beyond the pressure transducer. It could also arise partly from the tolerance on the pipe radius itself: a tolerance of 10% on the pipe radius could itself lead to a 45% difference in ΔP.

III. RESULTS AND DISCUSSION

A. Experimental results

We measure the pressure drop ΔP over time as material is injected into the pipe of radius R_0 and length L, at flow rate Q. As deposition occurs, a reduction in the pipe radius leads effectively to an increased shear rate inside the pipe; Table IV indicates the minimum shear rate as ~ 10 s^{-1}. As seen in the viscosity measurements in Fig. 1, increasing shear rates due to constriction can only decrease μ, albeit slightly, and thereby would not explain any observed increase in ΔP. Therefore,
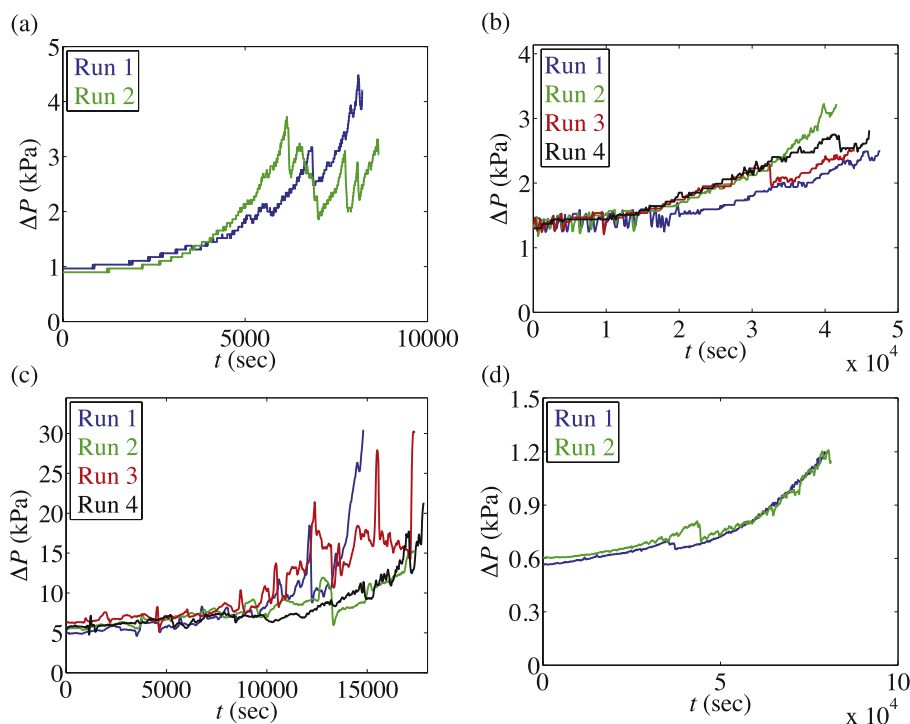

FIG. 4. Evolution of ΔP over time, showing typical run-to-run variations. (a) shows two runs of Mixture B (25% M2, 25% toluene, and 50% heptane by volume) at $Q = 40$ ml/h in Pipe 1. (b) and (c) show 4 runs each of Mixture C at $Q = 4.2$ ml/h in Pipe 1 and at $Q = 25.8$ ml/h in Pipe 3, respectively. (d) shows 2 runs of Mixture D at $Q = 6.6$ ml/h in Pipe 2.

all increases in ΔP reflect decreases in the pipe radius, signaling deposition. Typical experimental runs with asphaltene deposition look like those shown in Fig. 4. Each plot in Fig. 4 indicates the typical run-to-run variations seen in Mixture B (a), Mixture C ((b) and (c)), and Mixture D (d). In all cases, there is little change in the pressure drop at the beginning of the experiment. After some time, ΔP rises, but in a stochastic manner. The peaks and valleys in the traces of ΔP indicate some rearrangement in the deposit. In this sense, deposition could still be occurring throughout the pipe despite instantaneous decreases in ΔP that may signify local rearrangement events. Both runs of Mixture D in Pipe 2 exhibit such stochastic rearrangement events, as seen in Fig. 4(d), at $t < 5 \times 10^4$ s. In microfluidic visualizations of asphaltene deposition, this stochasticity was observed to be due to a stick-and-roll type behavior of the precipitated colloidal-scale asphaltenes.[14,15]

Despite the observed stochasticity, increasing the flow rate Q generally serves to alleviate deposition, given a constant pore-volume injection. This effect has been observed in both microfluidic experiments and in larger pipes ($R_0 \sim 12$ mm), but only when increasing Q by a factor of ~ 2.[11,14,15] In some cases, this effect has been referred to as "shear-limited deposition."[17] Fig. 5(a) shows three experimental traces of Mixture A at different flow rates, 40, 90, and 200 ml/h, all as a function of time. Because the runs are constant-volume injections, the fastest injection rate takes the shortest amount of time. Furthermore, as Q is increased, the overall deposition behavior is much less pronounced. To
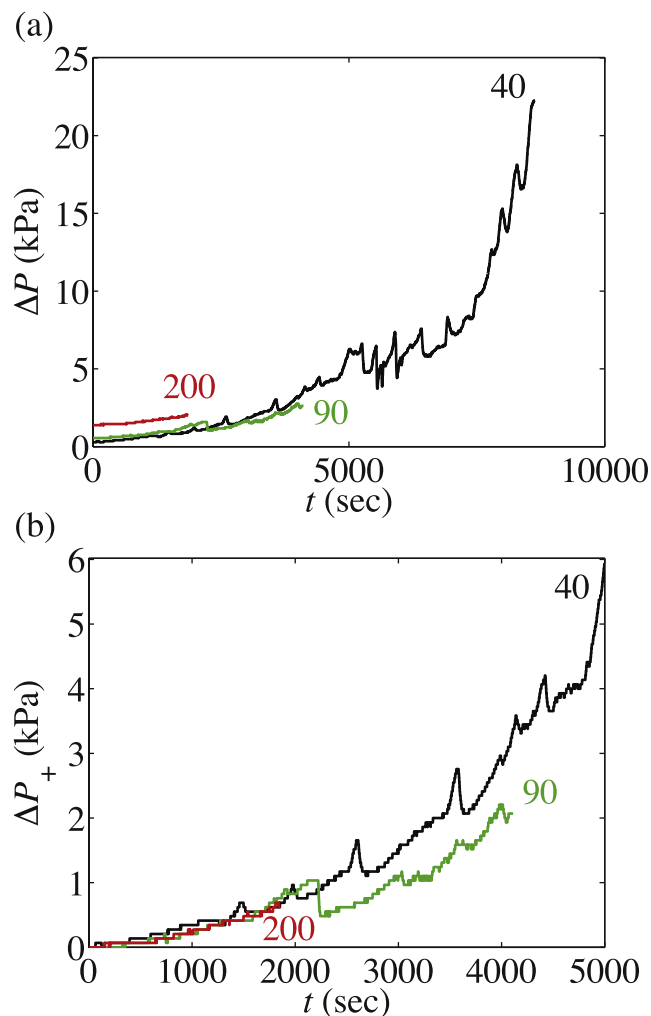

FIG. 5. Evolution of ΔP over time for three different values of Q. (a) shows raw data traces of Mixture A (M2 in equal volume with heptane) in Pipe 1. (b) shows the same data as in (a), but plotting the excess pressure drop ΔP_+, to illustrate the overlay of the traces. The three traces are labeled with the value of Q in ml/h. Note: Q is inversely proportional to the run duration in both (a) and (b).

compare runs at different Q with each other, we plot only the excess pressure drop due to deposition $\Delta P_+ = \Delta P - \Delta P_0$, as shown in Fig. 5(b). The traces of $\Delta P_+(t)$ at different values of Q overlay on top of one another for the full extent of the fastest run, $t < 2000$ s. Disregarding the stochastic event and almost instantaneous decrease in ΔP_+ at $t = 2170$ s for $Q = 90$ ml/h, the overlap is excellent. This collapse suggests the possibility for a universal scaling behavior.

We non-dimensionalize the time axis to pore volumes: $\tau = Qt/V$. In this way, we can assess the effect of flow rate Q on the overall deposition behavior. As seen in Fig. 6, increasing Q serves to decrease the overall deposition build-up. All four examples confirm the effect of Q, as with Mixture A [$f_p \sim 0.03$] in (a), Mixture B [$f_p \sim 0.02$] in (b), and Mixture C [$f_p \sim 0.05$] in both Pipe 1 (c) and Pipe 2 (d). This is seen most clearly in the case of Mixture C in Pipe 1, shown in Fig. 6(c). Due to the more than 2 order of magnitude difference in ΔP_+ between the $Q = 6$ and $Q = 200$ ml/h runs, the inset in Fig. 6(a) shows the traces at $Q = 90$ and 200 ml/h for Mixture A.

We assess compositional effects by comparing injections of Mixture A [$f_p \sim 0.03$] and Mixture B [$f_p \sim 0.02$] at the same values of Q and both in Pipe 1. When $Q = 6$ ml/h, the overall deposition in Mixture A causes ΔP_+ to rise to 160 kPa, while for Mixture B, ΔP_+ rises less than 7 kPa. This behavior is seen in Fig. 7(a). When Q is increased to 40 ml/h, still Mixture A exhibits a greater amount of deposition than Mixture B, but the overall effect is reduced due to the higher flow rate. This behavior is seen in Fig. 7(b). The effect of composition is apparent at each flow rate: Mixture A is composed of the pure petroleum fluid M2 mixed with heptane and asphaltene content $f_p \sim 0.03$, while the petroleum fluid component of Mixture B is M2 diluted with toluene in an equivolume ratio, resulting in $f_p \sim 0.02$. Mixture A, with the larger asphaltene fraction, therefore causes a greater amount of deposition regardless of Q.

The effect of pipe geometry can be seen when comparing injections of the same mixture into different pipes. By comparing Pipes 2 and 3, we assess the effect of length, and by comparing Pipes 1
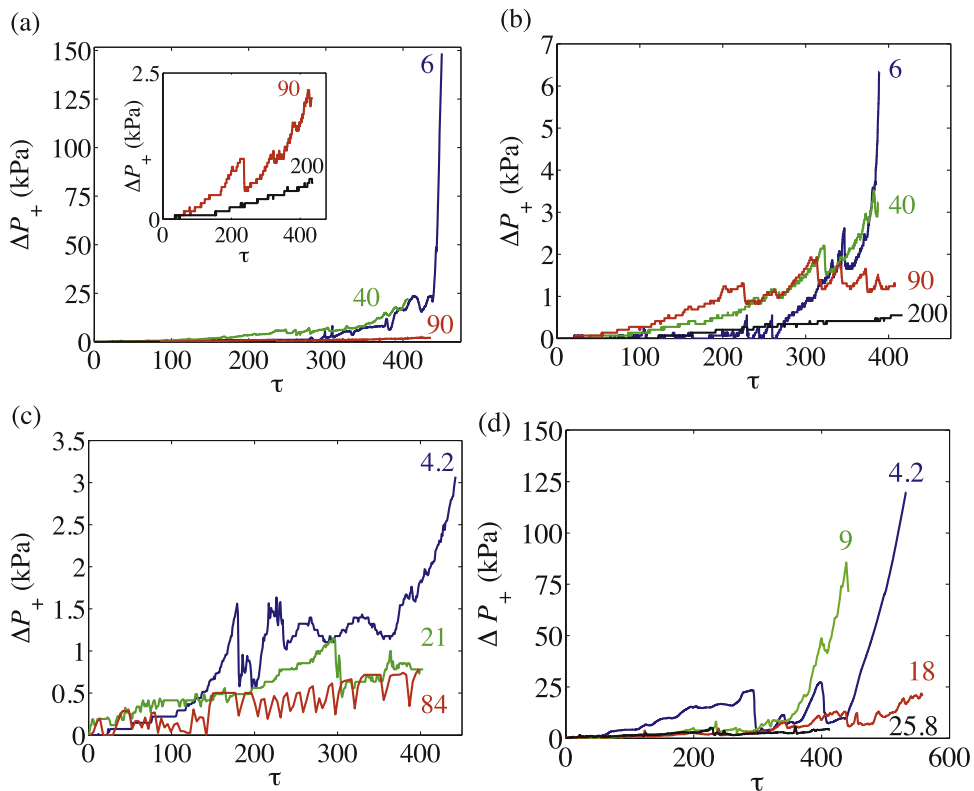

FIG. 6. Effect of Q on the evolution of ΔP_+ as a function of τ. (a) shows 4 values of Q for Mixture A in Pipe 1. The inset shows the runs at $Q = 90$ and 200 ml/h. (b) shows 4 values of Q for Mixture B in Pipe 1. (c) shows 3 values of Q for Mixture C in Pipe 1, and (d) shows 4 values of Q for Mixture C in Pipe 2. Each trace is labeled with Q in ml/h. Note: within each plot, Q is inversely proportional to the maximum value of ΔP_+ observed in each run.
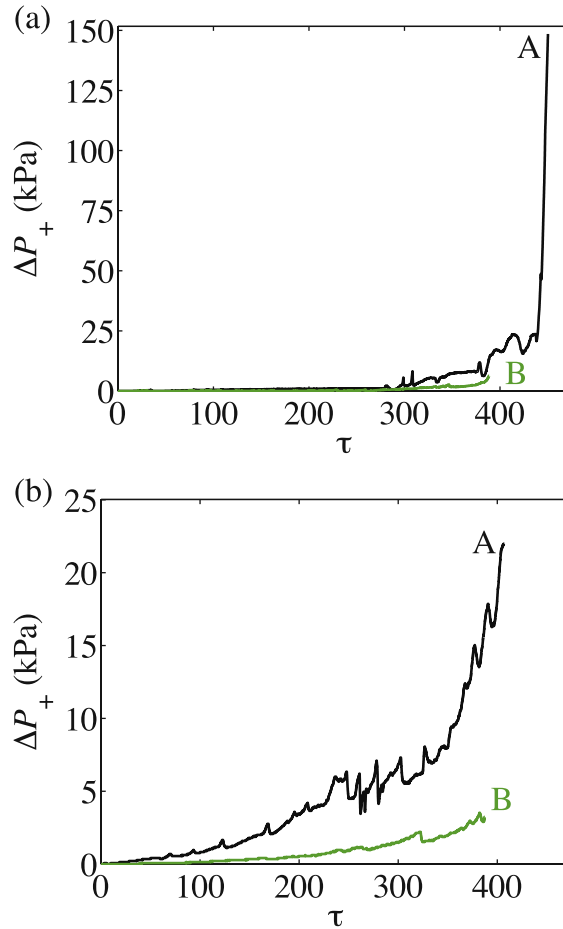
FIG. 7. Effect of ϕ and μ on the evolution of ΔP_+ as a function of τ. (a) shows Mixtures A and B in Pipe 1, both at $Q = 6$ ml/h. (b) shows Mixtures A and B in Pipe 1, both at $Q = 40$ ml/h.

and 2, we assess the effect of radius. Using Pipes 2 and 3, which both have inner radius $R_0 = 0.03$ cm, we find that in the limit $L \gg R_0$, the length of the pipe does not strongly affect the overall deposition behavior. As seen in Fig. 8(a), ΔP behaves similarly for an equal pore volume injection in each pipe. The effect of L is seen only before the onset of deposition: $L_3 \sim 2L_2$, and therefore, ΔP_0 is twice as large for the injection in the longer pipe. The excess length of Pipe 3 does not have a strong effect in increasing the deposition behavior, in agreement with other works in the literature.[16] The effect of radius on ΔP is much more pronounced, as expected given the dependence of ΔP on R_0 even in clean pipes, as in Eq. (2). Because $R_{0,1} \sim 2R_{0,2}$, there is an order of magnitude difference in the values of ΔP_0, before the onset of deposition. Therefore, we plot ΔP_+ for both Pipes 1 and 2 in Fig. 8(b).

We can compare the collection of 15 runs in Fig. 6 altogether by investigating the pressure increase at a given, fixed τ. We choose $\tau = 380$ and plot the normalized $\Delta P_{380}/\Delta P_0$ as a function of Q. As seen in Fig. 9, given the comparison at a fixed pore volume injection, increasing flow rate can drastically reduce deposition behavior. Fig. 9(a) shows the behavior of $\Delta P_{380}/\Delta P_0$ for the three Mixtures A [$f_p \sim 0.03$], B [$f_p \sim 0.02$], and C [$f_p \sim 0.05$], all injected in Pipe 1. As the flow rate increases from one run to the next, both the overall growth in ΔP and the deposition decrease. In fact, extending the Q axis beyond that shown in Fig. 9(a), we find that deposition is prevented entirely at $Q > 200$ ml/h, given $\tau = 380$ for Mixture C in Pipe 1, shown in Fig. 9(b).

B. Analysis

In assessing the theoretical behavior for deposition in a pipe of radius R_0, we first make a few simplifying assumptions. Given the high Peclet flows in the pipe, we assume convection-dominated
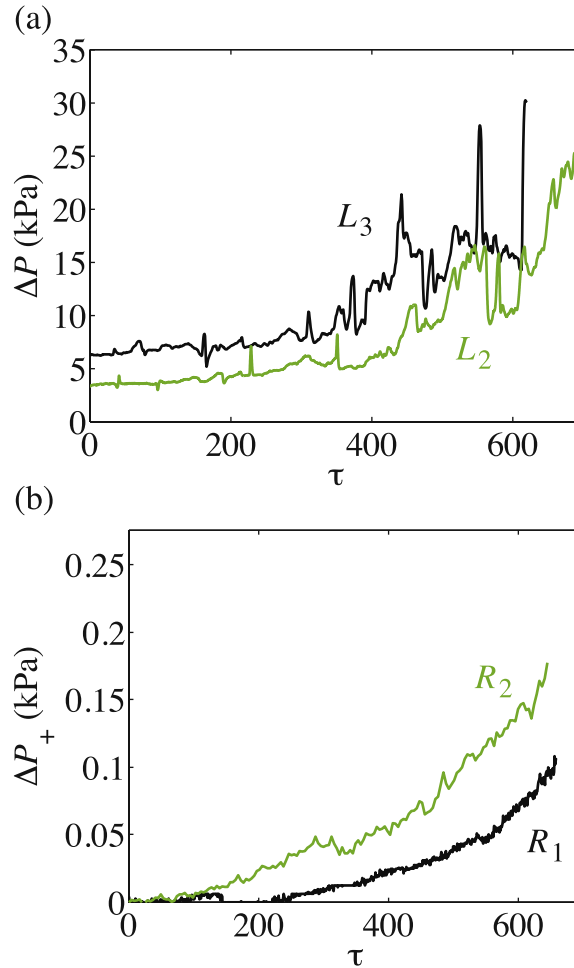
FIG. 8. Effect of pipe geometry on the evolution of ΔP. (a) shows ΔP as a function of τ, for injections of Mixture C in Pipes 2 and 3, where $L_3 \sim 2L_2$. Both traces in (a) are obtained at constant $Q = 25.8$ ml/h. (b) shows ΔP_+ for injections of Mixture D in Pipes 1 and 2, where $R_1 \sim 2R_2$. Both traces in (b) are obtained at constant $Q = 6.6$ ml/h.

conditions, with diffusion playing an important role near the boundary only, within $\delta \sim RPe^{-1/3}$ of the occluded pipe radius R.[21,22] The boundary layer thickness, δ, has a weak (1/3 power) dependence on the axial position, but we neglect this in our analysis. The mechanism of deposition is assumed to be driven by diffusion within the boundary layer δ, regardless of the molecular nature of the adhesive interactions between the asphaltenes and the pipe or the deposit. The deposit is assumed to be uniform in the axial and radial directions. The assumption of radial symmetry neglects gravity, which may play a role in large diameter horizontal pipes.

A volume of depositing material is injected through the pipe at a flow rate Q, which leads to clogging of the pipe, as assessed experimentally through the pressure drop ΔP. We will determine the scaling behavior for a deposit of thickness $\triangle(t)$ that builds up inside the pipe, leaving only an annulus of radius,

$$R(t) = R_0 - \triangle(t), \tag{3}$$

unobstructed, as shown in Fig. 10(a). The flow in the pipe is laminar, governed by Eq. (2). Given a mixture with precipitating asphaltene volume fraction ϕ, we assume that only a quantity $\kappa\phi$ will deposit on the pipe wall, where $\kappa < 1$, and signifies the percentage of asphaltene adhesion to the deposited layer. The parameter κ thus depends on the chemical properties of the asphaltenes. While ϕ can be predicted by using thermodynamic models and modified Hildebrand solubility parameters,[12,18] we measure ϕ directly and independently via the filtered asphaltene precipitate content f_P for each
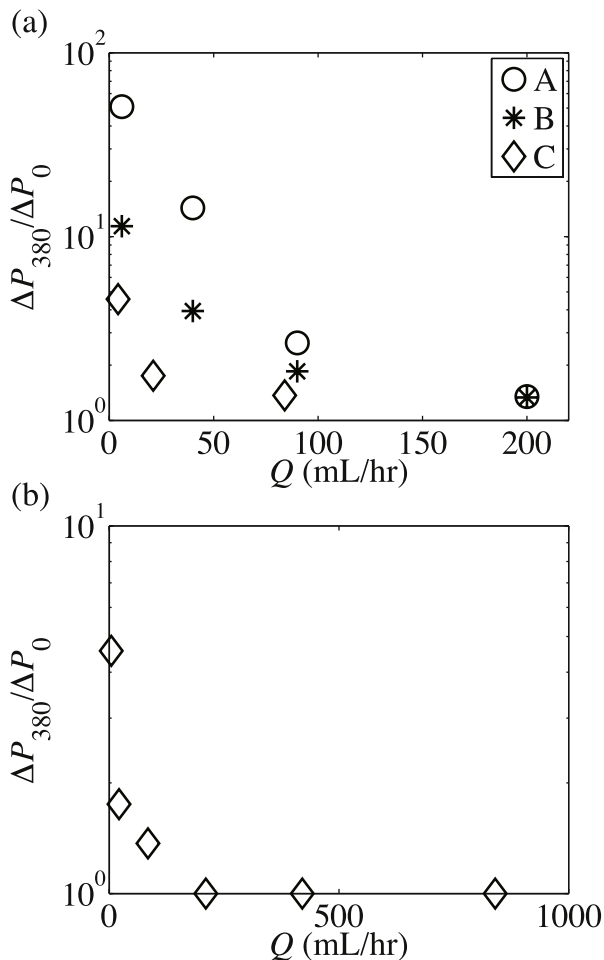
FIG. 9. Normalized pressure drop $\Delta P_{380}/\Delta P_0$ as a function of flow rate. (a) shows results for Mixtures A, B, and C, as listed in the legend. All measurements are from Pipe 1. (b) shows the complete inhibition of deposition at large enough Q for the given τ, as exemplified by Mixture C in Pipe 1. The results for each mixture are all obtained for a fixed pore volume injection $\tau = 380$.

of the petroleum fluid-heptane mixtures. By measuring f_p at the same temperature and compositions used in the pipe flow experiments, we thereby capture the thermodynamic considerations for our lab-scale system. We note that κ may depend in part on surface chemistry interactions between the pipe and the precipitated asphaltenes and thus is a quantity independent of the precipitated asphaltene fraction itself.
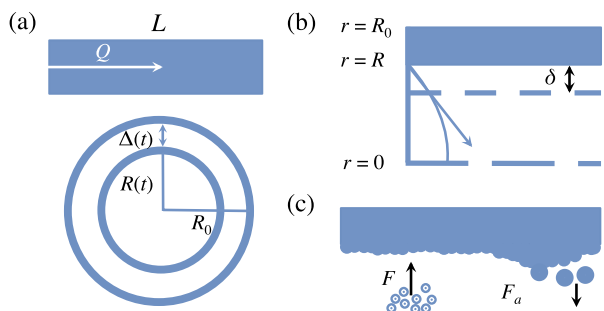

FIG. 10. (a) shows the direction of flow along the length of the pipe on top, with $R(t) = R_0 - \Delta(t)$ in cross section, below. (b) shows the velocity profile for fluid flowing in an annulus surrounded by a solid deposit, and (c) shows a cartoon of diffusive flux F perpendicular to the deposit balancing the flux F_a of ablated flocs being convected downstream.

The evolution equation for $R(t)$ is given by

$$\pi \frac{d}{dt}\left(R_0^2 - R^2\right) = 2\pi R F, \tag{4}$$

where F represents the flux of material toward the wall, with units of velocity. If all of the precipitated asphaltene materials entering the pipe were to deposit on the wall, we might expect $F = k\phi(Q/R^2)$. However, in the case of diffusion limited deposition within a thin boundary layer δ, F is determined by diffusion near the boundary,

$$F = -\kappa D \frac{d\phi}{dr} \sim \frac{kD\phi}{\delta}. \tag{5}$$

We use $\delta = cRPe^{-1/3}$, where in principal c has a weak dependence on L/R_0, but we take c to be a constant, consistent with neglecting the axial dependence of the deposited layer thickness. Thus,

$$F = \frac{kD\phi}{R}Pe^{1/3}, \tag{6}$$

where we define $k = \kappa/c$. Note that k absorbs the weak geometric dependence of c. Here, we assume that neither the occluded radius nor δ depend on the distance from the inlet. Due to the diffusive layer δ, F increases only gently with Q. Furthermore, given the inverse relationship between D and particle size a, small particles deposit more readily than do large particles. Given the range of Pe in our experiments, as in Table IV, we find $\delta <\sim 0.02R$, suggesting the diffusive boundary layer does not exceed 2% of the unoccluded pipe radius. This observation confirms that δ is small compared to R, and the approximation in Eq. (5) is valid. Substituting for F in Eq. (4), the build-up of the deposit is governed by

$$-R\frac{dR}{dt} = kD\phi Pe^{1/3}. \tag{7}$$

We non-dimensionalize $\bar{R} = R/R_0$ and use the dimensionless time $\tau = Qt/V$, where $V = \pi R_0^2 L$ is the volume of the pipe. Accordingly, we find

$$-\bar{R}\frac{d\bar{R}}{d\tau} = Bk\phi Pe^{-2/3}, \tag{8}$$

where $B = 2\pi L/R_0$. With this non-dimensionalization, we find the occlusion scales as $Q^{-2/3}$ and thus arrive at the well known result that an increasingly smaller amount of suspended material reaches the wall at higher flow rates in diffusion-limited deposition. The inverse is also true: low flow rates facilitate increasing deposition in the diffusive boundary layer. Integrating with the initial condition $\bar{R}(0) = 1$, we obtain

$$\bar{R}^2 = 1 - BkPe^{-2/3}\phi\tau. \tag{9}$$

Accordingly, the thickness of the deposit on the wall is given by $\triangle \approx \frac{1}{2}R_0 BkPe^{-2/3}\phi\tau$ and $\triangle \sim Q^{-2/3}$ for constant pore volume injections. We use Eq. (2) to obtain this result which we can compare to our measurements,

$$\Delta P = \Delta P_0 \frac{1}{(1 - BkPe^{-2/3}\phi\tau)^2}, \tag{10}$$

where $\Delta P_0 = 8\mu Q/\pi R_0^4$. Interestingly, Eq. (10) predicts a rise in ΔP that begins smoothly and immediately, contrary to suggestions of a "deposition detection time" or "induction period."[16,17] The complete clogging of the pipe generates a singularity in the flow, a complete obstruction, when $\bar{R} \to 0$. Clogging will always occur eventually, when

$$\frac{Bk\phi\tau}{Pe^{2/3}} \to 1. \tag{11}$$

As $Bk\phi\tau$ increases, as in higher asphaltene content fluids or for very large pore volume injections, a larger flow rate Q or larger Pe must be maintained to avoid severe clogging. Furthermore, this analysis reveals that the suppression of deposition at high flow rates, also observed here but described

elsewhere as "shear-rate limited" deposition,[17] simply reflects that the measured extent of τ is shorter than required for significant deposition. The diffusion-limited deposition model captures the effect of reduced deposition at large Q without need for a specific nomenclature to describe the high-Q regime.

In some cases, when the flow rate Q is low, we observe a smaller increase in ΔP than expected, which may be due to shear induced ablation of the deposited layer of asphaltenes.[13] In this case, ablation is not caused by a large overall flow rate Q, but rather by the locally high shear rate encountered as the deposit encroaches into the center of the channel. For instance, at the lowest flow rate run in Mixture A, $Q = 6$ ml/h, $Pe \sim 1.5 \times 10^6$, and $\phi \sim f_p = 0.03$. Assuming $k = 0.5$, complete clogging is expected at a pore volume injection $\tau \sim 400$, sending $Bk\phi\tau Pe^{-2/3} \to 1$ and $\Delta P \to \infty$, indicating complete clogging. However, given the constant flow rate output of the syringe pumps, complete clogging events are accompanied by experimental failure at the weakest point, namely, bursting of the tubing line junctures feeding the metal pipe. Despite reaching $P_+ \sim 150$ kPa at $\tau \sim 450$ in the $Q = 6$ ml/h run of Mixture A, as seen in Fig. 6(a), no experimental failure nor complete clogging was observed; the mixture continued to flow through the pipe until the entire injection volume was exhausted. Furthermore, the behavior of $\Delta P(\tau)$ in this $Q = 6$ ml/h run seems to follow the dynamics of the less-depositing, higher flow rate $Q = 40$ ml/h run below $\tau \sim 400$. Ablation by shear would explain a smaller extent of clogging than expected from Eq. (10). The slow overall flow rate Q facilitates diffusion-driven deposition with the fixed pore volume injection. As the deposit grows toward the center of the channel, the local shear rate $\dot{\gamma}$ increases, despite the slow overall flow rate. High local shear can rearrange or even remove portions of the deposit encroaching furthest into the center of the pipe. Furthermore, shear ablation has been observed in microscopy experiments assessing asphaltene deposition in microfluidic devices.[14,15] This balance of deposition and erosion also plays an important role in sediment growth and transport.[23]

As the deposited layer grows toward the center of the pipe, the local shear stress exerted on its surfaces $\mu\dot{\gamma}$ increases due to the increasing local shear rate,

$$\dot{\gamma} = \frac{Q}{R^3}, \tag{12}$$

and can limit the thickness of the deposited asphaltene layer. Under the assumption that the asphaltene deposit is composed of flocs that are weakly cohered by colloidal forces, the deposited layer may undergo shear ablation when subjected to stresses comparable to

$$\tau_d \sim \frac{nk_BT}{d^3}, \tag{13}$$

where d is the characteristic floc size removed by ablation and n is of order 1. In an alternative formulation, the deposit is assumed to have a pseudo-yield stress.[13]

To quantify the effect of ablation, we formulate a shear removal term to balance the diffusive flux toward the deposit. Fig. 10(c) shows a cartoon of the diffusive and ablative fluxes. The diffusive flux F toward the deposit is dominated by the diffusion of small asphaltene particles, whereas the ablative flux F_a consists of larger flocs being convected downstream after being broken away from the deposit. The magnitude of the ablative flux is determined by the ratio of local shear stresses to the internal colloidal stresses of the flocs in the deposit,

$$F_a \sim \frac{\mu\dot{\gamma}}{\tau_d}\dot{\gamma}d, \tag{14}$$

where $\dot{\gamma}d$ is the local fluid velocity carrying ablated portions downstream, and $\dot{\gamma}$ and τ_d are given in Eqs. (12) and (13). Like F, F_a scales as a velocity ($\dot{\gamma}d$), while the dimensionless ratio $\mu\dot{\gamma}/\tau_d$ gives the relative magnitude of the local shear stresses compared to the internal cohesive stresses holding the deposit together. At long times, the ablative and diffusive fluxes balance, giving a steady-state limit for the occluded radius,

$$\bar{R} = \bar{R}_\infty \quad \text{and} \quad \Delta P = \Delta P_\infty, \qquad \tau \to \infty, \tag{15}$$

where

$$\bar{R}_\infty \sim Pe^{1/9}\left(\frac{\mu Q d^4}{\phi n k_B T}\right)^{1/6} \tag{16}$$

and

$$\frac{\Delta P_\infty}{\Delta P_0} \sim Pe^{-4/9}\left(\frac{\mu Q d^4}{\phi n k_B T}\right)^{-2/3}, \tag{17}$$

according to Eqs. (5), (14), and (2). As seen in Eqs. (16) and (17), ablation depends on both the flow conditions, Pe and Q, and the mixture properties viscosity μ and asphaltene volume fraction ϕ. The ablation limit on ΔP depends most strongly on the size of the ablated flocs d and is also affected by the internal strength of the deposit, set by n. Because this limit is determined from a steady-state balance of fluxes, τ does not appear in Eq. (16) or Eq. (17). Contrary to suggestions in the literature of an upper limit on flow rate, beyond which deposition is suppressed, our analysis suggests a lower limit on flow rate, below which deposition becomes balanced by ablation, serving to limit further deposition.[17]

C. Comparison

To compare the prediction of the model with the experimental data, we rearrange Eq. (10),

$$\left(\frac{\Delta P}{\Delta P_0}\right)^{-1/2} = 1 - Bk\phi\tau Pe^{-2/3}. \tag{18}$$

If the build-up of the deposit is limited by diffusive transport toward the wall, in a flow regime where ablation by shear is unimportant, a rescaling of the raw data will yield a straight line when $(\Delta P/\Delta P_0)^{-1/2}$ is plotted with respect to $\tau Pe^{-2/3}$ for any individual run. The line should have a y-intercept of 1 and a slope with one value $Bk\phi$ for a given mixture, regardless of Q.

Indeed, when the experimental runs are rescaled as in Eq. (18), nearly all of the runs collapse to a line as anticipated. There are three exceptions, which will be discussed below, two of which indicate the importance of ablation by shear at low flow rates. Fig. 11 shows these results for Mixture A in (a), Mixture B in (b), and Mixture C in both Pipe 1 (c) and Pipe 2 (d). For both Mixtures A and B, the three runs at flow rates $Q = 40$, 90, and 200 ml/h rescale to a straight line. All three runs of Mixture C in Pipe 1 rescale to a straight line, as seen in Fig. 11(c), where the y-intercept = 1. For Mixture C in Pipe 2, the three larger Q runs also collapse to a straight line. For all three mixtures, the dashed black line denotes a fit to the collapsed data. Furthermore, each trace can be fit to yield values of k for each run, using the geometry of the pipes to determine B and the filtration results to estimate asphaltene volume fraction ϕ based on the precipitated mass fraction f_p. Table V summarizes the k values for each run. The best agreement between the values of k at different flow rates is seen in Mixture B [$f_p \sim 0.02$], which has a 6% spread in the individual values of k. For Mixture A [$f_p \sim 0.03$], the variation is 16%. Even in the case of Mixture C [$f_p \sim 0.05$] in Pipe 1, the spread in the values of k does not exceed 30%, despite a factor of 20 in the range of Q values. For Mixture C in Pipe 2, the variation in k is 16%.

We compare the effectiveness of asphaltene adhesion between the petroleum fluids by assessing the values of k in Table V. This comparison can show qualitative differences between the petroleum fluids: the exact value of k is governed by our choice of the depositing particle size, $a = 100$ nm, the one material parameter for which we have no *in situ* measurement. However, we can estimate particle size based on our previous light scattering results measuring the aggregation and growth of precipitating asphaltenes.[2,24] Asphaltenes precipitating from a variety of petroleum fluids, including those studied here, grow from the molecular scale to the order of 100 nm within just seconds of mixing the petroleum fluid with heptane, our asphaltene precipitant, and further to the micron scale after several minutes. Recall also that given $D \sim 1/a$. In diffusively driven deposition, smaller particles are more easily deposited than larger particles simply because they diffuse faster. We assume that larger particles do not deposit given both their aggregation dynamics and also given their diffusive behavior. Furthermore, when deposition is carried out in a Couette cell, deposition indeed ceases as
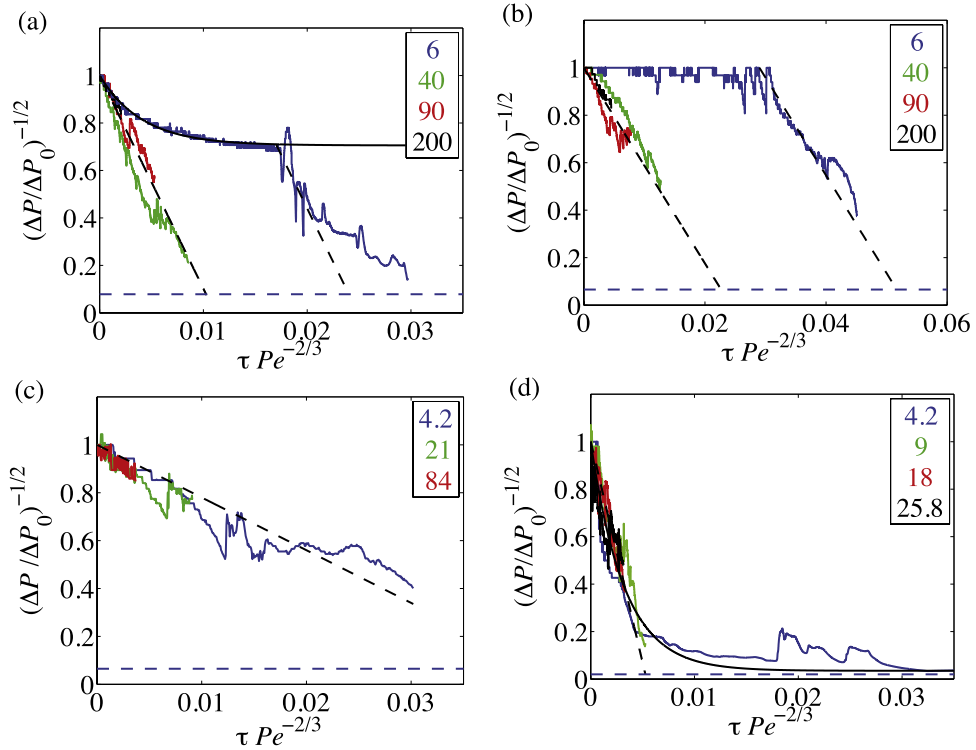
FIG. 11. Rescaling ΔP traces to extract parametric fits. (a), (b), and (c) show the rescaled raw data of ΔP for Mixtures A, B, and C, respectively, each in Pipe 1. (d) shows the rescaled raw data for Mixture C in Pipe 2. Each plot lists the flow rates Q in ml/h in their legends. The dashed black lines indicate linear fits to the rescaled data. The horizontal blue dashed lines indicate the steady-state limit determined by balancing diffusive deposition with shear ablation. In both (a) and (d), the solid black lines overlaid on the data indicate the functional form of the balance between deposition and ablation.

the particles grow to the micron scale during the course of the experiment.[13] Given all of these, we find choices for a between 50 and ~200 nm result in reasonable values for k, i.e. $k < 1$, suggesting $a = 100$ nm as a reasonable, intermediate value for the precipitating particle size.

The asphaltenes in Mixtures A and B are each derived from petroleum fluid M2. In Mixture B, the petroleum fluid is diluted with toluene by a volume factor 2 even before mixing with heptane, and as such, the quantity of precipitated asphaltenes in Mixture B [$f_p \sim 0.02$] is roughly 2/3 that as in Mixture A [$f_p \sim 0.03$]. Despite this difference in asphaltene content and the presence of toluene, the values of k for both Mixtures A and B are within ~ 20% of each other, with overlapping error bars: for Mixture A, $\langle k \rangle = 0.72 \pm 0.11$, while for Mixture B, $\langle k \rangle = 0.58 \pm 0.03$. While the presence of toluene in Mixture B changes the solubility of the asphaltenes, thermodynamic descriptions of this solubility are not required in this diffusively driven deposition model: all that is needed is the measurement of the precipitating asphaltene fraction from the mixture injected through the pipe, as provided in Table II. Mixture C, however, with [$f_p \sim 0.05$], is made of petroleum fluid CVA, with more than twice the asphaltene content of M2. Despite its larger asphaltene content, Mixture C has

TABLE V. Parameter k for Mixtures A, B, and C in Pipe 1 and for Mixture C in Pipe 2. The asphaltene fraction f_p is repeated for each mixture.

Mixture	f_p	Pipe	Q (ml/h)	k	Q (ml/h)	k	Q (ml/h)	k
A	0.0301 ± 0.0050	1	40	0.84	90	0.71	200	0.60
B	0.0190 ± 0.0031	1	40	0.55	90	0.61	200	0.57
C	0.0504 ± 0.0055	1	4.2	0.33	21	0.52	84	0.35
C	0.0504 ± 0.0055	2	9	0.25	18	0.33	25.8	0.28

a value $\langle k \rangle = 0.34 \pm 0.09$, indicating less effective adhesion of CVA asphaltenes onto the pipe. This comparison lends insight into the differences between the petroleum fluids: the asphaltenes from M2 must be more adherent to metal than those from CVA, and the dilution of M2 by toluene does not change this observation. The transport model neglects molecular asphaltene chemistry which cause adhesion and therefore does not account for chemical differences from one petroleum fluid to the next. It is interesting to note that the k values for Mixture C do not differ greatly between Pipe 1 and Pipe 2. In Pipe 1, $\langle k \rangle = 0.40 \pm 0.10$, while in Pipe 2, $\langle k \rangle = 0.29 \pm 0.04$. The overlap in the error bars suggests that the difference in pipe geometry does not adversely affect diffusively driven deposition model. Our assumptions of uniform deposition are reasonable and further supported by the images in Fig. 2(c) showing asphaltene deposit at the inlet, outlet, and intermediate cross sections of the pipe.

The three exceptional runs which do not collapse are the $Q = 6$ ml/h runs of Mixture A and Mixture B, as seen in Figs. 11(a) and 11(b), and the $Q = 4.2$ ml/h run of Mixture C in Pipe 2, as seen in Fig. 11(d). The rescaling argument in Eq. (18) applies only to deposition driven by diffusion, in the absence of any shear ablation or other means of removal. The upper limit on ΔP in Eq. (17) refers to the steady-state affect of ablation balanced by diffusion. The current scaling argument suggests a steady-state limit on ΔP and so does not predict dynamics as ablation becomes important. The horizontal blue dashed lines show the steady-state limits on $(\Delta P / \Delta P_0)^{-1/2}$ for $Q = 6$ ml/h, in Figs. 11(a) and 11(b), and for $Q = 4.2$ ml/h in Figs. 11(c) and 11(d), all as determined by Eq. (17). We assume a floc size $d = 500$ nm, to reflect the propensity of asphaltenes to aggregate to the colloidal scale.[2] Since the internal cohesion stress τ_d scales inversely with d^3, smaller flocs require larger stresses to be removed from the deposit. Therefore, the ablated floc size is relatively large. Electrostatic interactions have been shown to drive the aggregation of colloidal asphaltene particles in suspension, and so we choose $n = 5$ based on the assumption of electrostatic interactions holding the deposit together.[24,25] In a low dielectric medium like petroleum fluid, with dielectric constant $\epsilon \sim 2$, $E = e^2 / (4\pi \epsilon_0 \epsilon r) = 5 k_B T$ is sufficient to separate two oppositely charged particles by a distance $r \sim 6$ nm, where e is the elementary charge and ϵ_0 is the permittivity of free space.

The equilibrium balance between deposition and ablation suggests that runs performed at constant flow rate Q will eventually generate a plateau in the re-scaled pressure drop, as long as the pore volumes injected reach a sufficiently large value τ_{crit}. We can solve for τ_{crit} by setting $\Delta P / \Delta P_0$ in the equilibrium limit (Eq. (17)) to the deposition behavior given in Eq. (10). Doing so suggests a complicated dependence of τ_{crit} on the various material parameters of the mixture. However, the qualitative behavior of $\tau_{crit} Pe^{-2/3}$ can be assessed by inspecting Fig. 11. Traces at higher flow rates Q have a shorter extent due to the relatively constant amount of pore volumes injected τ for all runs. Because high flow rate traces have a shorter extent, they require larger values of $\tau Pe^{-2/3}$ before reaching the equilibrium balance indicated by the horizontal dashed lines. With all other material parameters fixed, as in comparing single traces within a panel of Fig. 11, $\tau_{crit} \sim Q^{2/3}$: larger pore volume injections are required to balance deposition with ablation. By comparing Figs. 11(a) and 11(b), we can see the importance of the precipitating asphaltene content. For Mixture A, with $f_p \sim 0.03$, the dashed line fit for the traces at flow rates $Q \leq 90$ ml/h appears to intersect the equilibrium limit near $\tau Pe^{-2/3} \sim 0.01$. For Mixture B, with $f_p \sim 0.02$, this intersection would occur at a larger value, $\tau Pe^{-2/3} \sim 0.02$. This suggests that, with all else being constant, mixtures with lower precipitating asphaltene content require larger pore volume injections not only to significantly deposit but also to reach the equilibrium balance with shear ablation. Because in general $\tau_{crit} \sim Q^{2/3}$ for the amount of pore volumes required to observe ablation, the effect of ablation is more evident at low flow rates, which is indeed where we observe it to occur.

Investigation of the dynamics at low flow rates, at $Q = 6$ ml/h for Mixture A in Pipe 1 and $Q = 4.2$ ml/h for Mixture C in Pipe 2, can suggest some potential mechanisms balancing the diffusive flux leading to deposition. In the $Q = 6$ ml/h run of Mixture A (Fig. 11(a)), the rescaling of ΔP begins in a linear fashion, following the black dashed line with $k = 0.72$ until approximately $\tau \sim 44$ pore volumes injected, corresponding to $\tau Pe^{-2/3} \sim 0.01$, at which point it begins to reach a smooth plateau. This plateau may suggest the action of ablation in limiting the build-up of the deposit. At $\tau > 215$, however, some stochastic behavior sets in and the deposit builds again. The stochasticity may indicate local rearrangements as previously ablated asphaltene flocs stick and roll and finally re-deposit. The rebuilding of the deposit at first follows the deposition dynamics seen
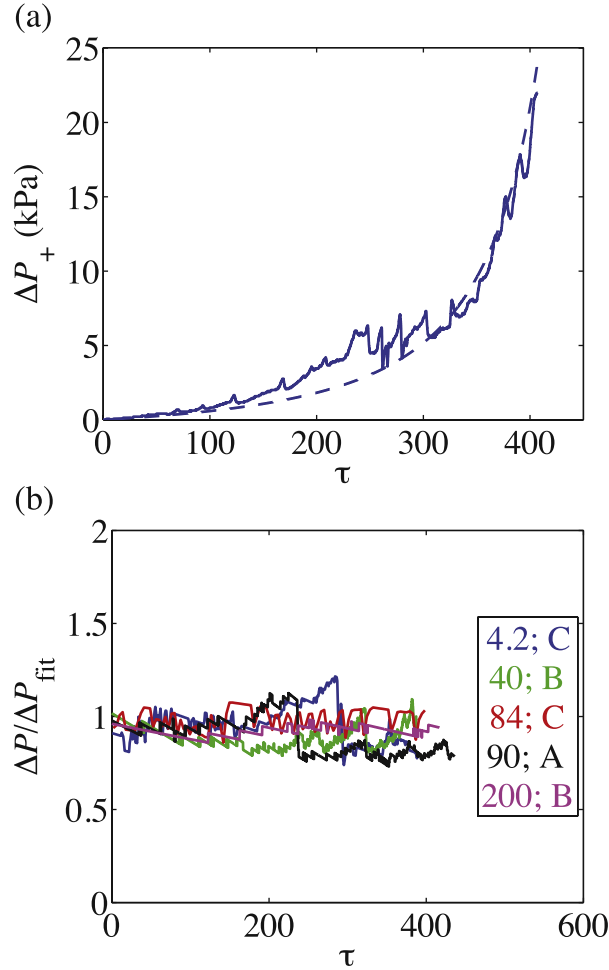
FIG. 12. Comparing experiments to the predictions. (a) shows an example fit of the data, for Mixture A injected in Pipe 1 at $Q = 40$ ml/h, using $B = 94.6$ as extracted from Fig. 11(a). The dashed line shows the predicted trace of ΔP_+. (b) shows $\Delta P / \Delta P_{fit}$ at five different values of Q as indicated in the legend, which includes the mixtures used, all in Pipe 1.

at flow rates $Q \geq 40$ ml/h, as indicated by the black dashed line shifted to $\tau Pe^{-2/3} = 0.017$ and $(\Delta P / \Delta P_0)^{-1/2} = 0.71$. A few additional ablative plateaus are seen at larger values of $\tau Pe^{-2/3}$, for instance near $\tau Pe^{-2/3} \sim 0.023$ and $\tau Pe^{-2/3} \sim 0.27$. Part of this stochastic re-deposition behavior may have to do with dynamical changes in the floc size as the deposit ages. In the case of Mixture C in Pipe 2, at a flow rate $Q = 4.2$ ml/h (Fig. 11(d)), the stochastic rearrangement events seem to happen at a somewhat larger scale and furthermore occur within the ablative plateau, as $\tau Pe^{-2/3} \sim 0.018$. Still, the rescaled traces approach, but do not cross, the steady-state ablation limits indicated by the horizontal blue dashed lines in both Figs. 11(a) and 11(d). Additional details beyond a scaling model at steady-state are required to predict dynamics which include stochastic and/or multiple ablation events.

The shapes of the traces exhibiting plateaus suggest a transition from pure deposition behavior at low values of $\tau Pe^{-2/3}$ to an equilibrium behavior where deposition is balanced by ablation. The lowest Q traces in Figs. 11(a) and 11(d) begin in a linear fashion for small $\tau Pe^{-2/3}$ and later reach a plateau. Given Eq. (18) as the short-time behavior and Eq. (15) for the long time limiting behavior, this suggests the form

$$\frac{\bar{R}^2 - \bar{R}_\infty^2}{1 - \bar{R}_\infty^2} = \exp\left(-\frac{Bk\phi Pe^{-2/3}\tau}{1 - \bar{R}_\infty^2}\right) \tag{19}$$
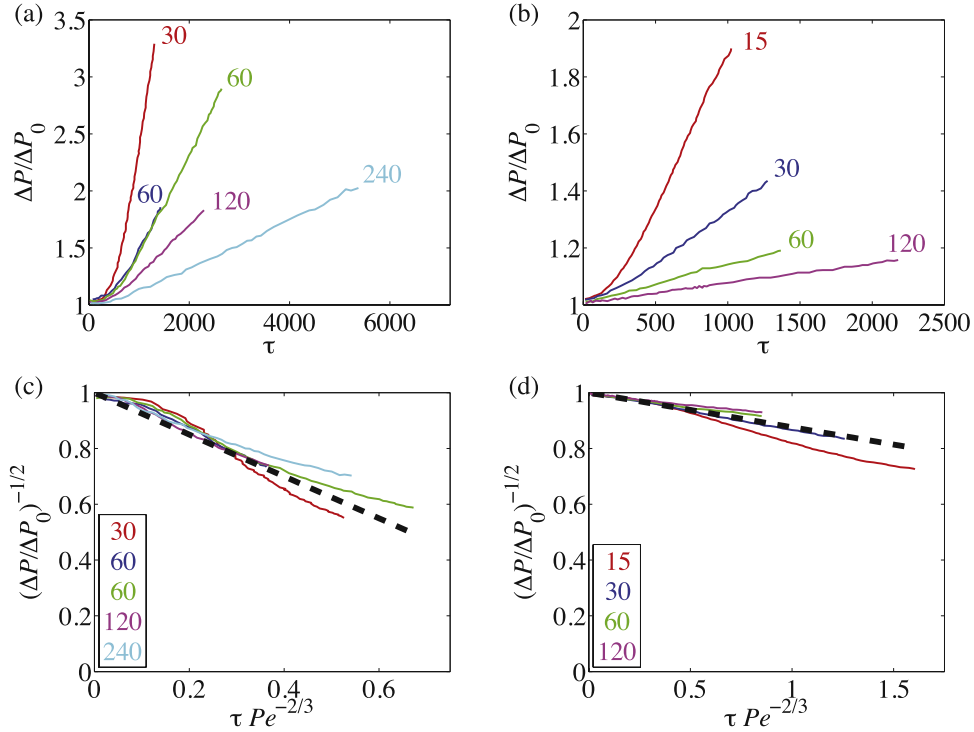
FIG. 13. Comparing experiments to the predictions. (a) and (b) show raw data from Nabzar and Aguilera.[17] (c) and (d) show the same data as in (a) and (b), respectively, rescaled by the model (dashed line fits) given in Eq. (18). In (a) and (b), the traces are labeled with Q in mL/h, while in (c) and (d) the legends indicate Q.

and correspondingly

$$\frac{\Delta P^{-1/2} - \Delta P_\infty^{-1/2}}{\Delta P_0^{-1/2} - \Delta P_\infty^{-1/2}} = \exp\left(-\frac{Bk\phi Pe^{-2/3}\tau}{1 - \bar{R}_\infty^2}\right) \tag{20}$$

by Eq. (2). The solid black lines overlaid on the lowest Q traces in Figs. 11(a) and 11(d) correspond to this functional form, where k is the fit to the initial linear slope, and $\bar{R}_\infty^2 = (\Delta P/\Delta P_0)^{-1/2}$ is obtained from the value of the plateau.

In the $Q = 6$ ml/h run of Mixture B, the situation is somewhat different. The rescaled trace of ΔP seems to remain unchanged on average until $\tau \sim 260$ pore volumes injected. After this, the rescaled ΔP seems almost to follow the same linear behavior as the higher three flow rates. Mixture B contains 25% by volume toluene. The stochastic deposition events recorded at $\tau Pe^{-2/3} <\sim 0.03$ in Fig. 11(b) suggest that the asphaltene deposits do not stick very strongly to the pipe during the first half of the run, and shear ablation is sufficient to keep the deposit fluid. As the deposit ages, the shear forces may not be sufficient to prevent deposition, and the clogging behavior returns at $\tau Pe^{-2/3} \sim 0.03$. Interestingly, this latency behavior does not alter the deposition dynamics. A second dashed black line, shifted to $\tau Pe^{-2/3} = 0.029$, indicates that the deposition still follows diffusion-driven dynamics.

Using the fitted values of k from Table V, we can predict the behavior of ΔP as a function of τ based on flow rate Q and the material and geometric parameters of the system. Fig. 12(a) shows such an example, using Mixture A in Pipe 1, at $Q = 40$ ml/h. The solid line shows the data, while the dashed line indicates the predicted behavior of ΔP_+. The discrepancies in the prediction arise from the stochastic nature of the deposition process. We quantify the stochasticity of the data through the ratio $\Delta P/\Delta P_{fit}$. As seen in Fig. 12(b), there are varying degrees of stochasticity when comparing runs against each other. The runs in Fig. 12(b) represent different values of Q as shown in the legend, for Mixtures C, B, C, A, and B, respectively. For all 12 runs collapsed in Fig. 11 that follow Eq. (18), the rms deviation from the fit ranges between 6% and 24%.
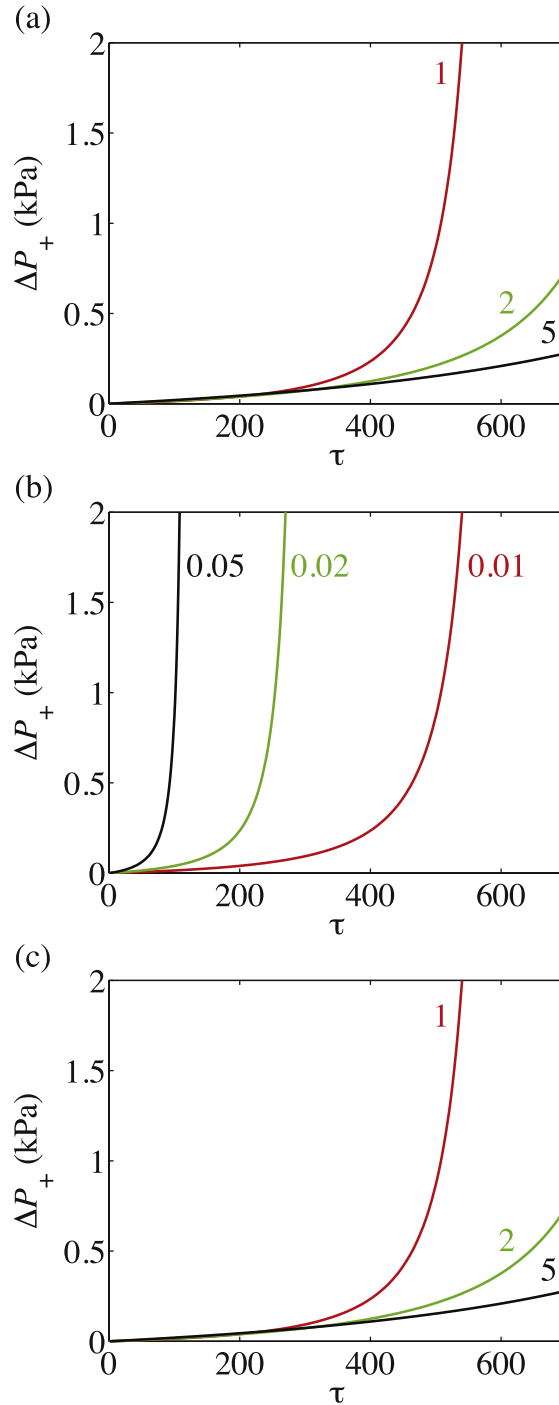
FIG. 14. Parametric effects in a pipe with $R_0 = 0.5$ mm. (a) shows the effect of Q on ΔP_+ for fixed $\phi = 0.01$ and $\mu = 1$ cp. The traces are labeled by the flow rates Q in ml/h. (b) shows the effect of ϕ on ΔP_+ as a function of pore volumes for fixed $Q = 1$ ml/h and $\mu = 1$ cp. The traces are labeled by the deposition volume fractions ϕ. (c) shows the effect of μ on ΔP_+ as a function of pore volumes for $Q = 1$ ml/h and $\phi = 0.01$. The traces are labeled by the fluid viscosities μ in cp.

To further validate our model, we compare with results in the literature. In particular, we can rescale raw data that are presented in terms of $\Delta P/\Delta P_0$ by using Eq. (18). Nabzar and Aguilera present $\Delta P/\Delta P_0$ for one depositing mixture in two different pipe geometries, using $L = 50$ cm with $R_0 = 0.26$ and 0.11 mm; however, they do not provide the precipitating asphaltene content ϕ.[17] We show the raw data from their Figs. 4(a) and 4(b) in Figs. 13(a) and 13(b), respectively. Figs. 13(c)

and 13(d) show the rescaled raw data according to Eq. (18), and the traces at different Q collapse to the expected linear behavior. Each trace in the collapsed data in Fig. 13(c) can be fit to a line, with slopes $\langle k\phi \rangle = 2.5 \pm 0.3 \times 10^{-4}$, for a variation of 13%. Likewise the traces in Fig. 13(c) can be fit with slopes $\langle k\phi \rangle = 1.0 \pm 0.3 \times 10^{-4}$, for a variation of 33%, comparable to the range of slopes seen in our own data. While the original data were described as exhibiting an "induction period," its collapse upon rescaling with our model shows instead that deposition begins immediately and is a continuous process.[17]

It is interesting to note that while the data from Nabzar and Aguilera extend farther in the dimension $\tau Pe^{-2/3}$ in Figs. 13(c) and 13(d), the clogging extent is considerably less than seen in our own data. The maximal decrease in $(\Delta P/\Delta P_0)^{-1/2}$ reaches ~ 0.6 in Fig. 13(c), and only to ~ 0.75 in Fig. 13(d). Our own depositing mixtures clog to a much greater extent, with all three mixtures reaching $(\Delta P/\Delta P_0)^{-1/2} \sim 0.4$, Mixture A reaching nearly $(\Delta P/\Delta P_0)^{-1/2} \sim 0.1$, and Mixture C in Pipe 2 nearing the ablation limit at $(\Delta P/\Delta P_0)^{-1/2} < 0.05$, all as seen in Fig. 11. The deposition model facilitates this type of comparison, which may be difficult to make by assessing raw data alone.

Given the agreement between the diffusive deposition model and the experimental data, we can use the model to understand the effects of the various material parameters in isolation, such as viscosity and asphaltene content, something that is not always possible in experiments. For instance, μ generally increases with ϕ for a real petroleum fluid, but investigation of the model can serve to tease out the individual effects of each parameter. To visualize the nonlinear parametric dependencies of Eq. (10), we fix $L = 30$ cm, $R = 0.05$ cm, $T = 25\,°\mathrm{C}$, and choose $k = 0.5$. In Fig. 14, ΔP_+ is plotted under a variety of conditions, and only one variable is allowed to vary in each plot: Q, ϕ, and μ. Keeping everything else constant, an increase in flow rate Q slows deposition, sweeping particles farther than δ from the wall before they have time to deposit, as seen in Fig. 14(a). An increase in the precipitated asphaltene volume fraction ϕ has a dramatic effect on increasing the rate of deposition, as the flux toward the wall is directly related to ϕ, as seen in Fig. 14(b). An increase in the suspending fluid viscosity μ slows deposition, as it lowers the diffusivity of the particles. This result may seem counterintuitive for petroleum fluids, since higher viscous petroleum fluids often have much larger volume fraction of asphaltenes leading to deposition. The red traces in Figs. 14(a)–14(c) all have identical conditions. In comparing the plots in Figs. 14(a)–14(c), each of which spans a factor of 5 in Q, ϕ, and μ, respectively, we find that the effect of Q and μ is identical: increases in Q and μ both lead to decreased deposition. By contrast, increasing ϕ increases the deposition behavior and has the greatest effect on the overall deposition behavior.

IV. CONCLUSIONS

We present a fluid dynamics and transport model which suggests that asphaltene deposition is governed by diffusively driven deposition which can be balanced against shear ablation at low flow rates. The model suggests that asphaltene deposition begins immediately and will result in significant clogging at any flow rate with a large enough pore-volume injection. The correspondence between the scaling model predictions and the experimental results suggests that theoretical arguments can be used to scale-up laminar flow results from the lab-scale to the field-scale. We assess the thermodynamics of asphaltene precipitation by measuring the precipitated asphaltene content and find that simple hydrodynamic and transport scaling arguments robustly predict asphaltene deposition. The success of the model suggests that purely hydrodynamic considerations can aid in the design of pipelines. Such scaling can also inform future lab-scale experiments, to help optimize the use of petroleum fluids in the lab, which are often a limited resource.

Interestingly, the diffusion-driven deposition process describes the overall dynamics well, despite its assumption of uniform deposition along the axial dimension of the pipe. The predictive agreement between the model and the experimental results, both our own and from the literature, suggests that the assumption of uniform deposition may not be a critical factor in predicting overall deposition behavior on these length scales. This interesting conclusion lends robustness to the simplicity of the diffusion-limited scaling model.

More important than the assumption of uniform deposition, perhaps, may be the understanding of asphaltene chemistry. While the current model does not take into account the interactions between colloidal asphaltenes and the metal pipe, the parametric fits provided by the model lend insight into the differences between asphaltenes from various sources. As seen through the comparison of the parameter k for Mixtures A, B, and C, the asphaltene source matters. M2, despite having a lower asphaltene content than CVA, actually exhibits a greater degree of its asphaltenes depositing on the pipe walls. In future investigations, we will use additive chemicals with known effects on asphaltene interactions to assess the possibilities for both chemical inhibition and removal of deposited asphaltenes.

Despite the complications presented by asphaltene chemistry, hydrodynamics and transport considerations alone can appropriately describe the physical process of asphaltene deposition. Our model predicts that low flow rates and high asphaltene content enhance deposition. In the experimental results, the low Q runs which should experience the most clogging are the same runs which reveal the importance of ablation by shear as the deposit grows toward the center of the pipe. Not only do our results shed light on the physical mechanisms involved in asphaltene deposition, but also the parametric scaling of the model may suggest certain universal design principles for field operations.

ACKNOWLEDGMENTS

[1] S. M. Hashmi, L. A. Quintiliano, and A. Firoozabadi, "Polymeric dispersants delay sedimentation in colloidal asphaltene suspensions," Langmuir **26**, 8021 (2010).

[2] S. M. Hashmi and A. Firoozabadi, "Effect of dispersant on asphaltene suspension dynamics: Aggregation and sedimentation," J. Phys. Chem. B **114**, 15780–15788 (2010).

[3] B. G. Prevo and O. D. Velev, "Controlled, rapid deposition of structured coatings from micro- and nanoparticle suspensions," Langmuir **20**, 2099 (2004).

[4] L. Malaquin, T. Kraus, H. Schmid, E. Delamarche, and H. Wolf, "Controlled particle placement through convective and capillary assembly," Langmuir **23**, 11513 (2007).

[5] R. Hansen, H. Bruus, T. H. Callisen, and O. Hassager, "Transient convection, diffusion, and adsorption in surface-based biosensors," Langmuir **28**, 7557 (2012).

[6] H. Shi, C. Kleinstreuer, Z. Zhang, and C. S. Kim, "Nanoparticle transport and deposition in bifurcating tubes with different inlet conditions," Phys. Fluids **16**, 2199 (2004).

[7] H. Shi, C. Kleinstreuer, and Z. Zhang, "Dilute suspension flow with nanoparticle deposition in a representative nasal airway model," Phys. Fluids **20**, 013301 (2008).

[8] C. E. Haskett and M. Tartera, "A practical solution to the problem of asphaltene deposits—Hassi Messaoud field, Algeria," J. Pet. Technol. **17**, 387–391 (1965).

[9] S. F. Alkafeef, F. Al-Medhahi, and A. D. Al-Shammari, "A simplified method to predict and prevent asphaltene deposition in oilwell tubings: Field case," SPE Prod. Facil. **20**, 126–132 (2005).

[10] E. Ramirez-Jaramillo, C. L. Galeana, and O. Manero, "Modelling asphaltene deposition in production pipelines," Energy Fuels **20**, 1184–1196 (2006).

[11] B. S. Soulgani, D. Rashtchian, B. Tohidi, and M. Jamialahmadi, "Integrated modelling method for asphaltene deposition in wellstring," J. Jpn. Pet. Inst. **52**, 322–331 (2009).

[12] F. Vargas, J. Creek, and W. Chapman, "On the development of an asphaltene deposition simulator," Energy Fuels **24**, 2294–2299 (2010).

[13] D. Eskin, J. Ratulowski, K. Akbarzadeh, and S. Pan, "Modelling asphaltene deposition in turbulent pipeline flows," Can. J. Chem. Eng. **89**, 421–441 (2011).

[14] E. S. Boek, H. K. Ladva, J. P. Crawshaw, and J. T. Padding, "Deposition of colloidal asphaltene in capillary flow: Experiments and mesoscopic simulation," Energy Fuels **22**, 805–813 (2008).

[15] A. D. Wilson, E. S. Boek, H. K. Ladva, J. P. Crawshaw, and J. T. Padding, "Recent developments in the deposition of colloidal asphaltene in capillary flow: Experiments and mesoscopic simulation," in 8th European Formation Damage Conference, Scheveningen, The Netherlands, 27-29 May 2009.

[16] M. P. Hoepfner, V. Limsakoune, V. Chuenmeechao, T. Maqbool, and H. S. Fogler, "A fundamental study of asphaltene deposition," Energy Fuels **27**, 725 (2013).

[17] L. Nabzar and M. E. Aguilera, "The colloidal approach. A promising route for asphaltene deposition modeling," Oil Gas Sci. Technol. **63**, 21–35 (2008).

[18] J. Wang, J. S. Buckley, and J. L. Creek, "Asphaltene deposition on metallic surfaces," J. Dispersion Sci. Technol. **25**, 1–12 (2004).

[19] W. C. K. Poon, L. Starrs, S. P. Meeker, A. Moussaid, R. M. L. Evans, P. N. Pusey, and M. M. Robins, "Delayed sedimentation of transient gels in colloid-polymer mixtures: Dark-field observation, rheology and dynamic light scattering studies," Faraday Discuss. **112**, 143–154 (1999).

[20] L. Starrs, W. C. K. Poon, D. J. Hibberd, and M. M. Robins, "Collapse of transient gels in colloid-polymer mixtures," J. Phys.: Condens. Matter **14**, 2485–2505 (2002).

[21] A. Acrivos and J. D. Goddard, "Asymptotic expansions for laminar forced-convection heat and mass transfer. Part 1. Low speed flows," J. Fluid Mech. **23**, 273–291 (1965).

[22] C. R. Robertson and A. Acrivos, "Low Reynolds number shear flow past a rotating cylinder. Part 2. Heat transfer," J. Fluid Mech. **40**, 705–718 (1970).

[23] O. Duran, B. Andreotti, and P. Claudin, "Numerical simulation of turbulent sediment transport, from bed load to saltation," Phys. Fluids **24**, 103306 (2012).

[24] S. M. Hashmi and A. Firoozabadi, "Tuning size and electrostatics in non-polar colloidal asphaltene suspensions by polymeric adsorption," Soft Matter **7**, 8384 (2011).

[25] S. M. Hashmi and A. Firoozabadi, "Controlling nonpolar colloidal asphaltene aggregation by electrostatic repulsion," Energy Fuels **26**, 4438 (2012).